

ARTICLE

DOI: 10.1038/s41467-018-03761-4

OPEN

Immiscible hydrous Fe–Ca–P melt and the origin of iron oxide-apatite ore deposits

Tong Hou^{1,2}, Bernard Charlier³, François Holtz¹, Ilya Veksler^{4,5}, Zhaochong Zhang², Rainer Thomas⁴ & Olivier Namur^{1,6}

The origin of iron oxide-apatite deposits is controversial. Silicate liquid immiscibility and separation of an iron-rich melt has been invoked, but Fe–Ca–P-rich and Si-poor melts similar in composition to the ore have never been observed in natural or synthetic magmatic systems. Here we report experiments on intermediate magmas that develop liquid immiscibility at 100 MPa, 1000–1040 °C, and oxygen fugacity conditions (f_{O_2}) of $\Delta FMQ = 0.5\text{--}3.3$ (FMQ = fayalite-magnetite-quartz equilibrium). Some of the immiscible melts are highly enriched in iron and phosphorous \pm calcium, and strongly depleted in silicon (<5 wt.% SiO₂). These Si-poor melts are in equilibrium with a rhyolitic conjugate and are produced under oxidized conditions ($\sim FMQ + 3.3$), high water activity ($a_{H_2O} \geq 0.7$), and in fluorine-bearing systems (1 wt.%). Our results show that increasing a_{H_2O} and f_{O_2} enlarges the two-liquid field thus allowing the Fe–Ca–P melt to separate easily from host silicic magma and produce iron oxide-apatite ores.

¹Institute of Mineralogy, Leibniz Universität Hannover, 30167 Hannover, Germany. ²State Key Laboratory of Geological Process and Mineral Resources, China University of Geosciences, 100083 Beijing, China. ³Department of Geology, University of Liege, 4000 Sart Tilman, Belgium. ⁴GFZ German Research Center for Geosciences, Telegrafenberg, 14473 Potsdam, Germany. ⁵Geological Department, Perm State University, Bukireva 15, Perm, Russia 614990. ⁶Department of Earth and Environmental Sciences, KU Leuven, 3001 Leuven, Belgium. Correspondence and requests for materials should be addressed to T.H. (email: thou@cugb.edu.cn)

The origin of orebodies composed of low-Ti iron oxide minerals (magnetite and/or hematite) and apatite in (sub) volcanic rocks is controversial^{1–12}. These rocks, essentially free of silicates and sufficiently enriched in Fe to be recoverable, have been classified as Kiruna-type or iron oxide-apatite (IOA) deposits^{1–3}. Their enrichment in Fe and P has been variously attributed to magmatic and hydrothermal ore-forming processes. Metasomatic replacement of the host igneous rocks by convecting fluids^{4,6}, proposed as a likely mechanism due to the pervasive hydrothermal alteration of the ore, is supported by the low Ti content and trace element characteristics of magnetite crystals^{4,9,10}. Alternatively, IOA deposits may represent volcanic flows or shallow magma intrusions as suggested by several field relationships including discordant veins and dykes of magnetite-apatite ores intruding their host rocks, magma flow structures, vesicular textures, and volcanic bombs^{5,7}. In this case, the formation of Fe-rich and P-rich rocks might be explained by liquid immiscibility and segregation of a Fe–P-rich immiscible magma from its rhyolitic counterpart⁷. The development of immiscibility is supported by the coexistence of two types of melts in glassy matrices and inclusions hosted by phenocrysts in the ore and in andesitic wall rocks^{7,11,13,14}. However, none of these immiscible melts have compositions representative of IOA ores. Experimental evidence for the formation of such silica-poor iron oxide melts at magmatic conditions is also lacking^{15,16}.

Evolved basaltic magmas can split into immiscible rhyolitic (dacitic) and ferrobasaltic melts along their crystallization path at temperatures below 1040–1020 °C^{17–19}. P₂O₅ in the bulk composition promotes the development of silicate liquid immiscibility and this oxide strongly concentrates in the Fe-rich melt^{16,20,21}. Experimental and natural Fe-rich immiscible melts generally contain 35–45 wt.% SiO₂ and only a few wt.% P₂O₅^{18,19,21–28}.

Silicate phases predominantly crystallize from such melts^{18,19}, producing oxide-apatite gabbros of moderate economic interest^{29,30}. Extreme enrichment of apatite and iron oxide over silicate minerals, as observed in IOA deposits, cannot simply result from differential crystal settling in an iron-rich silicate melt. This is because, with the exception of plagioclase, common silicate minerals (actinolite and diopside) are denser than the melt and would sink along with the oxides. A more efficient mechanism for the production of IOA deposits would be direct crystallization of a Fe–P-rich and Si-depleted magma.

Here, we provide an original solution to this challenging issue based on results obtained from experiments performed in realistic conditions of pressure and temperature in an internally heated pressure vessel (IHPV). We used experimental starting material which was prepared from a series of mixtures between two mafic end-members and a rhyolitic composition (Supplementary Fig. 1 and Supplementary Tables 1, 2). We show that liquid immiscibility develops in the intermediate magmas at conditions relevant to the magmatic reservoirs of most subvolcanic IOA deposits ($P = 100$ MPa, $T = 1000$ – 1040 °C). With elevation of oxygen fugacity and water activity, nearly pure Fe–Ca–P melts that are compositionally identical to typical IOA ores are produced by liquid immiscibility. This finding allows us to conclude that liquid immiscibility is the key process in the formation of IOA deposits. This is extremely important for the establishment and refinement of a petrogenetic model for IOA ores.

Results

Phase equilibria and immiscibility textures. Experimental conditions and phase assemblages are summarized in Supplementary Table 3. All run products contain crystal phases and either a

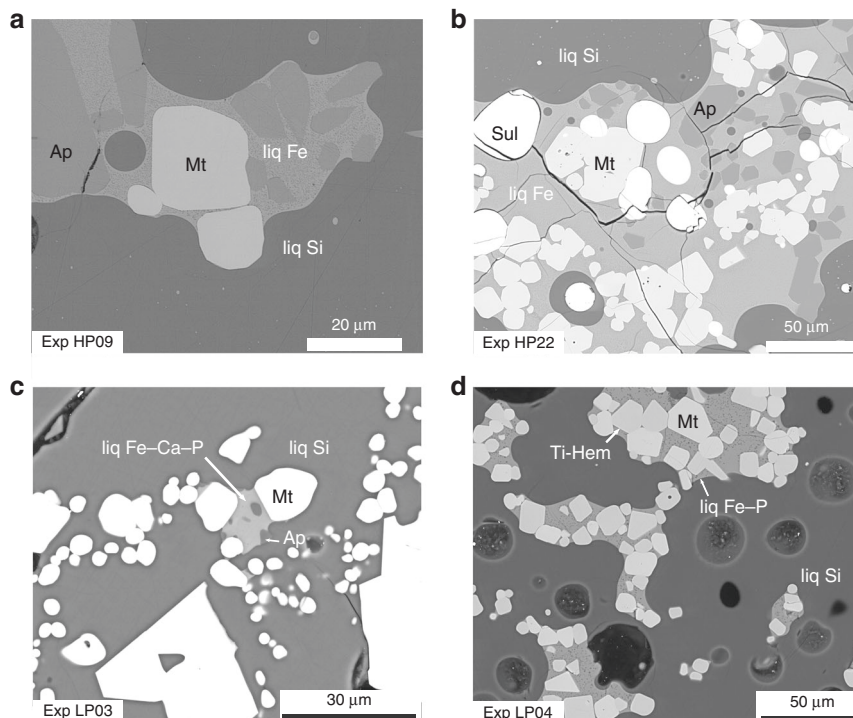


Fig. 1 Back-scattered electron images of selected experiments showing liquid immiscibility between Fe-rich and Si-rich glass. **a, b** Typical irregularly shaped (coalesced) patches of Fe-rich silicate glass (liq Fe) within Si-rich glass (liq Si). Magnetite and/or apatite are preferentially enclosed in the immiscible Fe-rich silicate glasses. **c** Fe–Ca–P glass (liq Fe–Ca–P) separated from the Si-rich glass (liq Si). Magnetite and apatite are crystalline phases in both liquids. **d** Irregularly shaped (coalesced) patches of Fe–P glass (liq Fe–P) within Si-rich glass. Oxide minerals (Ti-rich hematite and magnetite) are predominantly hosted by the Fe–P glass. Abbreviations: Mt, magnetite; Ti-Hem, solid solution of ilmenite and hematite; Ap, apatite; Sul, sulfide; liq Fe, Fe-rich silicate glass; liq Fe–Ca–P, Fe–Ca–P glass; liq Fe–P, Fe–P glass; liq Si, Si-rich glass

single homogenous melt or two distinct immiscible melts quenched to glass. Solid phases are magnetite, apatite, fayalite (or fayalitic olivine), a silica phase (tridymite), and occasionally titanohematite and clinopyroxene. A single homogeneous melt is found in some experiments with high bulk P_2O_5 contents (1.1–2.3 wt.% P_2O_5 ; Supplementary Table 2), indicating that, despite the critical role of phosphorus on the development of liquid immiscibility³¹, other compositional parameters must contribute significantly to the onset of unmixing. We note that a single melt is also observed in experiments performed at the highest temperature (i.e., 1040 °C) suggesting that in our multi-component system the apex of the binodal lies beneath 1040 °C, as already identified in dry ferrobasalts¹⁹. We also note that all experiments performed below 1040 °C under oxidizing conditions (fayalite-magnetite-quartz equilibrium) (\sim FMQ + 3) developed immiscibility while some experiments performed at identical temperature under more reduced conditions do not show immiscibility.

Experimental products with distinct immiscibility typically show sharp two-liquid interfaces (Fig. 1). Immiscible melts form globules or domains of various sizes (including nano-scale

droplets). We observe no compositional difference between small and large melt pools in individual experiments, suggesting complete equilibration of the two melts. In runs with sufficiently large globules, the Fe-rich melt droplets display very small wetting angles with magnetite, apatite, and fayalite, and these phases form euhedral crystals preferentially concentrated in the Fe-rich melt (Fig. 1). Experiments in which we added an FeS component (HP22–27) also contain large spherical or ovoid droplets of sulfide melt dispersed in the silicate glasses: our experimental products therefore contain three immiscible liquids (Fig. 1b).

Olivine and oxide mineral compositions. Electron microprobe analyses of the crystal phases are presented in Supplementary Data 1. Olivine compositions vary from Fo_{24} to Fo_2 ($Fo = 100$ [Mg/(Mg + Fe²⁺)]) with decreasing fO_2 and temperature. Under oxidizing conditions (FMQ + 3.1 to FMQ + 3.3), experiments contain two oxide minerals (Fig. 1d), a rhombohedral oxide of the hematite-ilmenite solid solution (14.84–24.64 wt.% TiO_2) and magnetite (0.38–1.53 wt.% TiO_2). Under more reducing

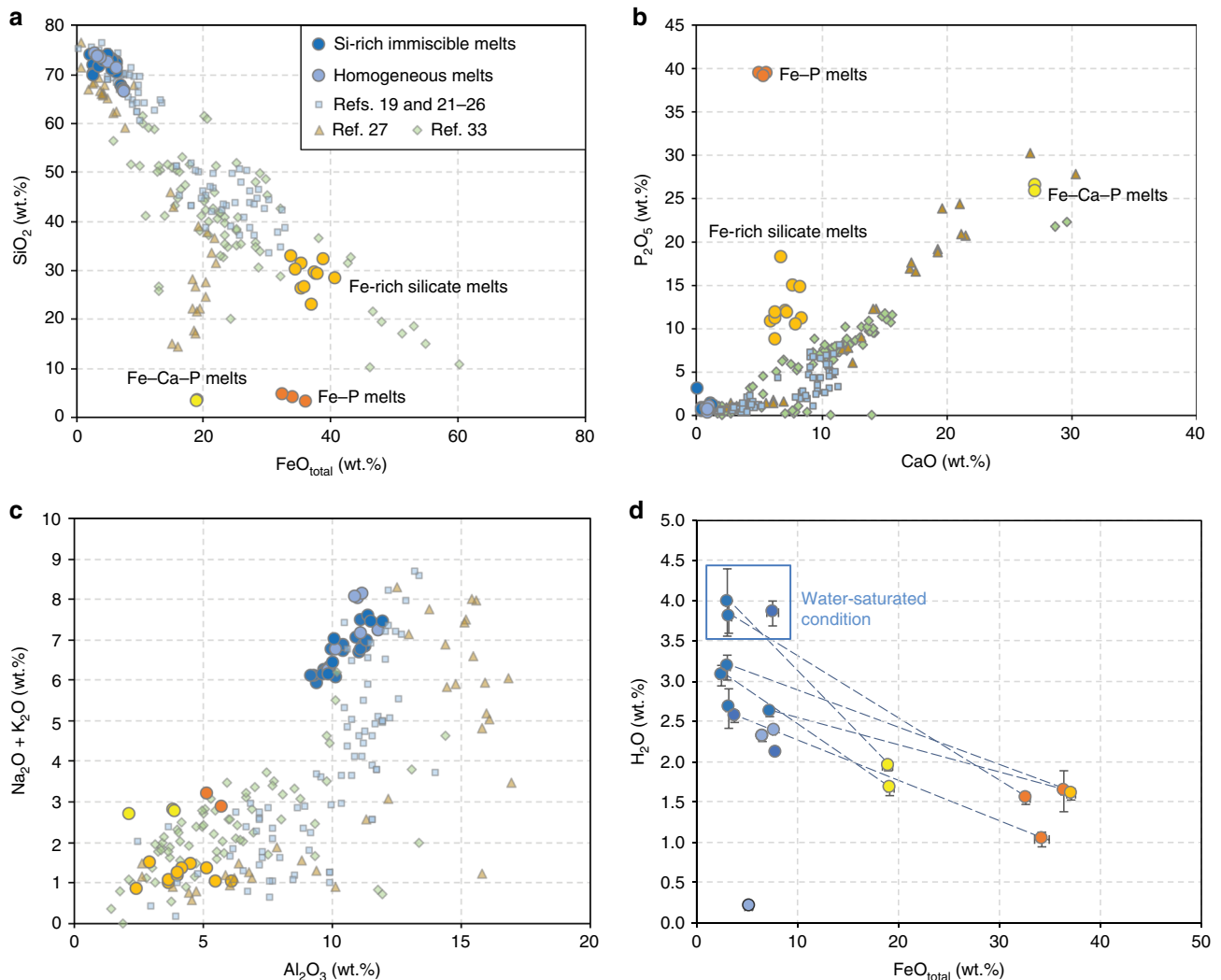


Fig. 2 Compositional variations of the experimental melts: **a** FeO_{tot} vs. SiO_2 ; **b** CaO vs. P_2O_5 ; **c** Al_2O_3 vs. $Na_2O + K_2O$; and **d** H_2O vs. FeO_{tot} . Three types of Fe-rich immiscible melts were produced: Fe-rich silicate melts and Fe-P and Fe-Ca-P melts. Literature data are plotted for comparison: Fe-rich melts in the mesostasis of natural samples³³, mineral-hosted melt inclusions²⁷, and experimental immiscible melts in tholeiitic systems^{19, 21–26}. Error bars represent one standard deviation of replicate analyses

Table 1 Compositional ranges of melts in this study

Liquid pairs	SiO ₂	TiO ₂	Al ₂ O ₃	FeO _{tot}	MnO	MgO
Fe-rich silicate melts	22.69–32.66	0.81–2.82	2.44–6.14	33.85–40.84	0.99–2.73	1.48–4.21
Si-rich conjugates	67.63–72.94	0.20–0.56	9.65–11.36	4.53–7.21	0.13–0.27	0.20–0.55
Fe–P melts	3.09–4.55	0.99–1.53	2.18–3.90	32.63–36.36	2.99–3.28	4.87–5.22
Si-rich conjugates	70.97–73.71	0.54–0.60	9.22–9.69	2.48–3.20	0.06–0.12	0.12–0.16
Fe–Ca–P melts	3.33–3.40	0.98	5.19–5.72	18.88–19.15	3.53–5.66	7.23–7.48
Si-rich conjugates	73.23–74.13	0.68–0.73	9.42–9.98	2.99–3.05	0.15–0.21	0.25–0.33
Si-rich melts with nano-scale Fe-rich globules	66.55–73.90	0.26–0.52	9.85–11.98	3.73–7.74	0.05–0.27	0.05–0.62
Homogeneous Si-melts (no immiscibility)	66.43–74.16	0.24–0.35	9.90–11.80	3.13–7.70	0.14–0.35	0.27–0.62
Liquid pairs	CaO	Na ₂ O	K ₂ O	P ₂ O ₅	F	
Fe-rich silicate melts	6.02–8.49	0.57–0.83	0.25–0.69	8.55–18.07	0.23–0.41	
Si-rich conjugates	1.00–1.40	1.73–2.48	4.17–4.99	0.44–1.09	0.10–0.17	
Fe–P melts	5.13–5.74	1.74–1.90	0.77–1.00	39.02–39.40	0.48–0.60	
Si-rich conjugates	0.15–0.21	1.47–1.86	3.95–4.23	2.84–2.96	0.31–0.69	
Fe–Ca–P melts	27.16–27.20	2.19–2.50	0.65–0.69	25.71–26.43	2.51–2.71	
Si-rich conjugates	0.52–0.74	1.69–2.20	4.21–4.54	0.37–0.62	0.15–0.17	
Si-rich melts with nano-scale Fe-rich globules	0.51–1.37	1.92–2.43	4.20–5.16	0.30–1.00	0.10–0.19	
Homogeneous Si-melts (no immiscibility)	0.95–1.19	2.08–3.29	4.15–4.89	0.20–0.89	0.09–0.17	

conditions (FMQ + 0.5), the oxide phase is magnetite (Supplementary Data 1).

Melt compositions. Experimental melt compositions are reported in Supplementary Data 1 and illustrated in Harker diagrams (Fig. 2). Depending on bulk compositions and experimental conditions, we observe three types of sulfur-free Fe-rich immiscible melts defining a broad compositional range: a Fe-rich silicate melt similar to a ferrobasalt, a Fe–P melt, and a Fe–Ca–P melt (Fig. 2; Table 1). Fe-rich silicate melts contain 22.7–32.7 wt.% SiO₂, 33.9–40.8 wt.% FeO_{tot}, 8.6–18.1 wt.% P₂O₅, and are enriched in MgO, CaO, and TiO₂. Most Fe-rich silicate melts were produced under nominally dry conditions (Supplementary Table 3). Fe–P melts were produced under relatively oxidizing (FMQ + 3.1 to FMQ + 3.3) and hydrous conditions ($a_{\text{H}_2\text{O}} = 0.7\text{--}1.0$). They are homogenous and contain 32.6–33.4 wt.% FeO_{tot}, 39.0–39.4 wt.% P₂O₅, with minor SiO₂ (3.1–4.6 wt.%), TiO₂ (1.0–1.5 wt.%), Al₂O₃ (2.2–3.9 wt.%), MgO (4.9–5.2 wt.%), and CaO (5.1–5.7 wt.%). Fe–Ca–P melts, produced under water-saturated and oxidizing conditions (FMQ + 3.2 to FMQ + 3.3), contain 18.4–19.2 wt.% FeO_{tot}, 27.2–33.4 wt.% CaO, 23.8–26.4 wt.% P₂O₅, 7.2–7.5 wt.% MgO, minor SiO₂ (3.3–5.1 wt.%), TiO₂ (0.4–1.0 wt.%), and Al₂O₃ (5.2–5.7 wt.%), and have relatively high F contents (2.5–2.7 wt.%).

Conjugate Si-rich immiscible melt compositions vary from dacite to rhyolite, and are compositionally similar to felsic rocks hosting some IOA deposits (Fig. 3)^{32–37}. They contain 67.6–74.1 wt.% SiO₂, 9.2–11.4 wt.% Al₂O₃, 2.5–7.7 wt.% FeO_{tot}, 4.0–5.0 wt.% K₂O, and 1.5–2.5 wt.% Na₂O. The Si-rich immiscible melts equilibrated with Fe–P and Fe–Ca–P melts contain relatively little CaO (0.1–0.2 and 0.5–0.7 wt.%, respectively), whereas those equilibrated with Fe-rich silicate melts contain 1.0–1.4 wt.% CaO (Table 1). Silicate melts in experiments without liquid immiscibility are rhyolitic, and do not differ significantly from those coexisting with a Fe-rich liquid, suggesting that they are close to the binodal surface (Supplementary Data 1). Sulfide droplets have compositions close to stoichiometric FeS.

In water-saturated experiments, Si-rich melts contain more than 3.5 wt.% H₂O, whereas the Fe-rich conjugates usually contain less than 2 wt.% H₂O (Fig. 2d). This indicates that water preferentially partitions into the Si-rich liquids as also observed in water-unsaturated experiments. Volatile element distributions between the conjugate melts are described using partition

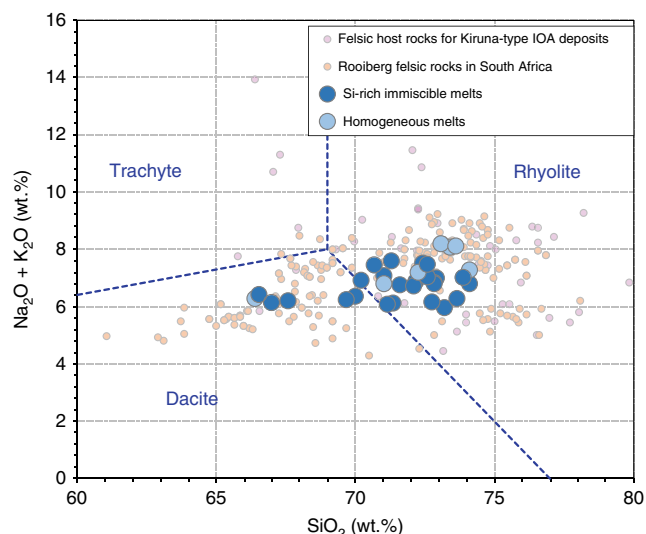


Fig. 3 TAS diagram showing the experimental dacitic and rhyolitic Si-rich melts. These immiscible Si-rich melts are similar to natural felsic rocks hosting Kiruna-type IOA deposits^{34–37} and those of the Rooiberg Group in South Africa³⁸

coefficients defined as $D_i = C_i^{\text{LFe}}/C_i^{\text{LSi}}$, where C represents the concentration (wt.%) of component i in the Fe-rich (LFe) and Si-rich (LSi) conjugate liquids. Liquid–liquid $D_{\text{H}_2\text{O}}$ values range from 0.39 to 0.69. F and SO₃ are enriched in the Fe-rich melts. D_{F} is about 2. This is consistent with our previous study in the F-rich multicomponent system²⁸, but contrasts with experimental results in simplified systems¹⁶ in which F was reported to partition nearly equally between the mafic and silicate liquids ($D_{\text{F}} = 1 \pm 0.6$). Due to the differences of the degree of melt polymerization in the immiscible conjugates³⁸, SO₃ partitions preferentially into the Fe-rich melts (Fe-rich melt: 1.07–1.53 wt.% SO₃; D_{SO_3} : 21.5–38.3) and sulfur concentrations in the Si-rich immiscible melts are therefore very low (0.03–0.06 wt.%).

Discussion

Several experimental studies in multi-component systems have reported immiscible melts. In most cases, the Fe-rich melts have

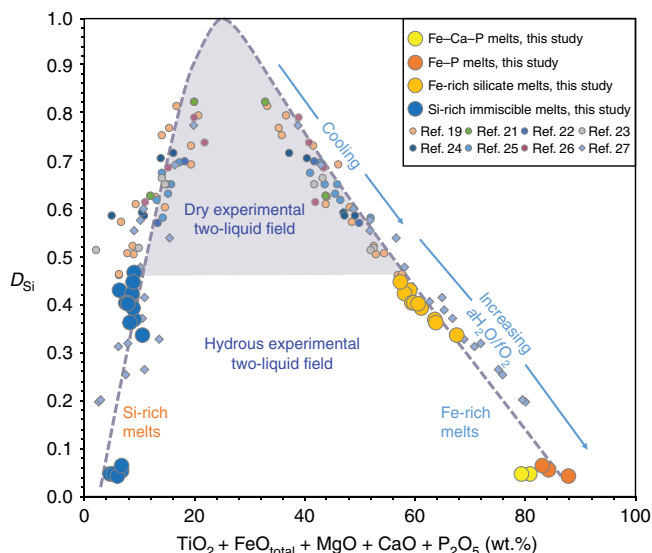


Fig. 4 Compositions of conjugate immiscible melts in this study compared to previous experimental melt pairs in tholeiitic systems^{19, 21–26} and native iron-hosted melt inclusions in lavas of the Siberian Traps²⁷. D_{Si} , the partitioning of SiO_2 between the Fe-rich and Si-rich melts, expresses the compositional gap between the two melts, plotted as a function of elements partitioned into the Fe-rich melts

at least 30 wt.% SiO_2 ^{19,21–26} (Fig. 4). With cooling, immiscible melt pairs become increasingly contrasted in composition, but dry Fe-rich melts reported so far have never approached the extreme, Si-free, composition of IOA ores (predominantly iron, calcium, phosphorous, with minor magnesium and titanium). The most extreme Fe–Ca–P-rich and Si-poor compositions reported to date (15 wt.% SiO_2 ; 22 wt.% FeO_{tot} ; 27 wt.% CaO ; 5–30 wt.% P_2O_5) have been observed in native iron-hosted immiscible melt pools from the Siberian Traps for which the conditions of formation are uncertain²⁷. They are, however, known to have equilibrated at extremely reduced redox conditions (close to IW) which are unrealistic for the formation of IOA deposits. These inclusions nevertheless indicate that Fe-rich immiscible melts in natural systems may become extremely enriched in Fe, Ca, and P, and depleted in Si (Fig. 4), although the compositions observed in Siberia still do not match the compositions of IOA ore deposits.

At the most reducing conditions investigated in our study, FMQ + 0.5, the dry Fe-rich immiscible melts produced in our experiments contain 23–33 wt.% SiO_2 (Table 1). These compositions are comparable to native iron-hosted melt inclusions but were produced at redox conditions more relevant to the formation of IOA ore deposits. With increasing $a\text{H}_2\text{O}$, immiscible pair compositions become more contrasted (Fig. 4). In water-saturated experiments, we also observe high P_2O_5 contents in Fe-rich silicate immiscible melts (up to 18.07 wt.%), which indicates that addition of H_2O into magmatic systems of intermediate composition enhances the development of immiscibility and expands the width of the binodal surface compared to that in dry systems (Fig. 4). We believe that even more contrasted compositions than those reported in this study could be produced at temperatures <1000 °C.

At more oxidizing (FMQ + 3.1 to FMQ + 3.3) and hydrous conditions, immiscible pair compositions are extremely contrasted compared to the liquids produced at FMQ + 0.5 and the Fe-rich melt has very little silica (Fig. 4). The major element partition coefficients between the two liquids are highly correlated with the degree of polymerization of the Si-rich melt²⁰. With increasing $f\text{O}_2$, $\text{Fe}^{3+}/\text{Fe}^{2+}$ increases in the Si-rich melt, which

becomes more polymerized because Fe^{3+} is a network former whereas Fe^{2+} is a network modifier³⁹. Consequently, immiscible pair compositions become more contrasted. In addition, the conjugate Fe-rich melt contains more Fe^{3+} , which substitutes for Si^{4+} via the reaction $\text{P}^{5+} + \text{Fe}^{3+} \leftrightarrow 2\text{Si}^{4+}$. Thus, increasingly hydrous and oxidizing conditions can explain the formation of Fe–P-enriched silicate liquids (Fig. 4), which is consistent with the recent studies on El Laco deposit¹¹.

Fluorine also plays an important role on the development of liquid–liquid immiscibility²⁸. Fluorine complexing with Mg in the melt⁴⁰ decreases the activity of MgO, therefore increasing the activity of FeO and favouring the development of liquid immiscibility²⁸. Fe–Ca–P melts contain more F (avg. 2.6 wt.%) compared to Fe–P melts (0.6 wt.%; Supplementary Data 1). We therefore suggest that fluorine also complexes with Ca⁴¹, such that addition of F produces Ca-enriched Fe–P melts. This implies that changing F in the parental magmas prior to immiscibility may lead to a range of Fe–P-dominated melts with variable amounts of calcium when immiscibility develops. Such a mechanism could account for contrasted amounts of apatite in different IOA deposits, i.e., from almost fluorapatite-free to the fluorapatite-rich deposits that are currently mined.

Our experiments produced several types of Fe-enriched and P-enriched immiscible melts. In particular, the composition of the Si-depleted and Fe–Ca–P-enriched melts is relevant to IOA ore production. These liquids are in equilibrium with typical dacites and rhyolites commonly observed to host IOA ores^{32–37}. However, the formation of such contrasted immiscible melt pairs, that could potentially form ore deposits, requires hydrous and oxidizing environments. In contrast to tholeiitic magmatism, these conditions are to be expected for IOA ores for two main reasons. First, IOA deposits are commonly located in convergent settings where slab dehydration leads to the formation of water-bearing magmas⁴². There are also commonly observed in extensional intraplate setting where crustal rocks melting^{43,44} may also produce hydrous magmas¹⁰. Second, the redox state of arc magmas is usually considered to be close to FMQ + 1, which is more oxidized than tholeiitic magmas⁴⁵. Further oxidation of the magma is likely to occur during crustal assimilation and magma degassing. Indeed, systematic O–Sr–Nd isotopic studies of IOA ores suggest a significant crustal component⁴⁶. Interactions with sediments such as carbonates or evaporites significantly oxidize magmas by decarbonatization and CO_2 fluxing or addition of S^{6+} from assimilated gypsum^{11,46}. As vapor-saturated magmas degas during ascent, the release of H_2O and CO_2 from the silicate melt further oxidizes the magma^{47,48}. Degassing of sulfur species can either oxidize or reduce the magma depending on the valence state of sulfur in the melt (S^{2-} or S^{6+}) and the fluid phase (H_2S or SO_2). In IOA deposits, sulfur dissolves in the melt predominantly as S^{6+} as supported by the common presence of anhydrite⁴⁶. Thus, sulfur degassing can lead to significant oxidation of the melt following the reaction SO_4 (melt) + 2FeO (melt) = SO_2 (gas) + Fe_2O_3 (melt) + $1/2\text{O}_2$ (melt). In addition, SO_2 is increasingly favored over H_2S since the following equilibrium shifts to the left with decreasing pressure⁴⁹: $\text{SO}_2 + 3\text{H}_2 = 2\text{H}_2\text{O} + \text{H}_2\text{S}$. Therefore, sulfur degassing leads to a continuous increase of $\text{Fe}^{3+}/\text{Fe}^{2+}$ in magmatic melts during decompression. The formation of IOA ore is thus intimately related to the emplacement dynamics of the host magmatic system: the parental intermediate magma is emplaced at shallow pressure, interacts with host sediments, and degasses. These processes produce oxidation of the magma that triggers immiscibility and the formation of Fe–Ca–P melt which further crystallizes to form IOA ores at the level of emplacement. In addition, crystallizing magnetite and apatite grains are preferentially wetted by the immiscible Fe-rich melt (Fig. 1). This may further enrich the crystal +

Fe-rich melt mush in elements of economic interest. Complete crystallization of the mush products leads to the formation of IOA ore.

Methods

Starting material synthesis. To prepare the synthetic mafic end-members, high-purity, commercially available oxide powders (SiO_2 , TiO_2 , Al_2O_3 , Fe_2O_3 , MnO , and MgO) were mixed with ethanol in an automatic agate mortar and pestle for more than 5 h. The rhyolitic composition was prepared from high-purity oxides and carbonates, and homogenized in an agate planetary ball mill. The powder mixture was then melted in a Pt crucible at 1600 °C (atmospheric oxygen fugacity) for 3 h. The glass was then ground in a steel mortar and re-melted in the furnace (1600 °C, 3.5 h) to homogenize the material and promote complete CO_2 degassing. After quenching, pieces of the glass were separated, mounted in epoxy, polished, and analyzed by electron microprobe (Supplementary Table 1).

Starting compositions were prepared from a series of mixtures between two mafic end-members and a rhyolitic composition (Supplementary Fig. 1 and Table 1–2). The two mafic end-members are mixtures of fayalite and magnetite in the proportions 30:70 (M1) and 60:40 (M2). Phosphorous was added as $\text{Ca}_3(\text{PO}_4)_2$ to them in various concentrations. To simulate the volatile-rich nature of IOA deposits, 2–6 wt.% H_2O was added to the starting compositions for some experiments. Because fluorapatite and sulfur-rich minerals are common in IOA deposits, all experiments contained 0.4–0.6 wt.% F, added as CaF_2 , and three experiments contained 3 wt.% S, added as FeS (Supplementary Table 2).

Phase equilibria experiments. All experiments were performed at 100 MPa in large volume IHPV⁵⁰ at the Leibniz University of Hannover (Germany). Starting powders were weighed and placed in Au capsules (20 mm length and 2.8 mm internal diameter, with a 0.2 mm wall thickness). One end of each capsule was welded shut before the starting material was inserted. The other capsule end was immediately welded shut for dry samples, whereas water-bearing samples were frozen in liquid nitrogen before welding. This method minimizes water vaporization during welding. Capsules were weighed after welding and placed in a dry furnace at 150 °C for 1–2 h before being re-weighed to check if any material loss occurred. During the experiments, the capsules were fixed to a Pt-wire in the hot spot of a double-wire element furnace. Temperature was controlled using two S-type thermocouples while two additional S-type thermocouples were used to monitor the sample temperature. The temperature gradient across the sample was less than 5 °C. Samples were pressurized cold to ~80% of final pressure, then heated to the final temperature while pressure was slowly increased. Temperature was increased with a ramp of 0.8 °C/s to 30 °C below the final temperature, and then 0.3 °C/s to the final temperature (1000–1040 °C). Experiments were run for 48–168 h, then quenched by fusing the Pt-wire and dropping the capsules onto a cold (~25 °C) copper block at the bottom of the sample holder. The quench rate was ~150 °C/s. Re-weighing of the capsules after the experimental runs showed identical weights for most capsules, indicating that no volatiles were lost during the experiments. Several chips of each experimental product (about 2 mm in diameter) were prepared as polished thin sections or mounted in epoxy for observation and electron microprobe analyses.

Oxygen fugacity calculations. Experiments were performed at $f\text{O}_2$ ranging from FMQ + 0.5 to FMQ + 3.3, in order to investigate the effect of changing redox conditions on resulting phase equilibria.

For experiments at intrinsic $f\text{O}_2$ conditions, we used an IHPV with Ar as the sole pressure medium. The intrinsic oxygen fugacity in capsules with pure H_2O fluid (mole fraction of water in the fluid $X_{\text{H}_2\text{O}}^{\text{fluid}} = 1$) in the IHPV used in this study was determined by NiPd-solid sensors⁵¹ at 1200 °C and 200 MPa. The obtained $f\text{O}_2$ corresponds to NNO + 2.6 (± 0.5 ; 1σ from microprobe analyses of the NiPd alloy) where NNO refers to the Ni–NiO buffer⁵². This corresponds to 3.3 log units above the FMQ solid oxygen buffer (hereafter labeled FMQ + 3.3). The $f\text{O}_2$ at H_2O undersaturated conditions can be estimated using the relation $\log f\text{O}_{2\text{capsule}} = \log f\text{O}_2$ (at $a_{\text{H}_2\text{O}} = 1$) + 2 $\log a_{\text{H}_2\text{O}}$ ^{53,54}, where $a_{\text{H}_2\text{O}}$ is determined from the water concentration in the melt following the model of ref. ⁵⁵. The overall error in the determination of the $f\text{O}_2$ in each experiment is estimated to be ~0.2 log units⁵³. For experimental runs conducted under nominally dry conditions (no fluid added), we assumed an $a_{\text{H}_2\text{O}}$ of 0.1 because such experiments are not strictly water-free for two reasons: (1) it is nearly impossible to avoid adsorbed water on the surface of the glass grains, and (2) hydrogen can be present in the pressure medium (gas) and may diffuse through the noble metal capsules. Thus in nominally dry experiments the silicate melts contained small amounts of water mainly present as OH groups (~0.3–1.0 wt.% depending on pressure and the extent of crystallization⁵⁶). In nominally dry experiments, the oxygen fugacity was estimated at ~FMQ + 0.5.

Other experiments performed at reduced conditions were conducted in an IHPV pressurized with a mixture of Ar and H_2 gases (the maximum H_2 pressure given in the IHPV before heating was 7.5 bar). Hydrogen diffuses through the noble metal inside the capsules. If water is present in the experimental charge, the oxygen fugacity is controlled by the equilibrium reaction for water formation ($\text{H}_2 + \text{O}_2 = \text{H}_2\text{O}$). As a result, at a given $f\text{H}_2$, the $f\text{O}_2$ decreases with decreasing water activity in the experimental charge. The calculation of $f\text{O}_2$ is based on the equation

of ref. ⁵⁷ [for further details see ref. ⁵³]. The $f\text{H}_2$ prevailing in the IHPV at high P and T was controlled with a Shaw membrane⁵⁰. Various oxygen fugacities were obtained by varying the proportions of H_2 and Ar in the pressure medium. We estimate that the overall error in the calculated $f\text{O}_2$ is about 0.2 log units.

Imaging and chemical analyses. Back-scattered electron images of the experimental run products were acquired on the QEMSCAN FEI Quanta 650F at RWTH Aachen (Germany). Chemical analyses were performed using a CAMECA SX100 electron probe microanalyser at the University of Hannover (Germany). Analyses were performed with an accelerating voltage of 15 kV. For silicate glasses, we used a beam current of 8 nA and a defocused beam of 10–20 μm . For sulfide liquids, we used a beam current of 15 nA and a defocused beam of 2–20 μm . Mineral analyses were performed with a beam current of 15 nA and a focused beam (1 μm). For minerals, the counting times were 15–20 s on peak for each element. The peak counting times for glasses were 10 s for Si, Ti, Al, Fe, Mn, Mg, Ca, and S, and 8 s for alkalis. The elements Na, K, Si, Ca, and Fe were measured first. Subsequent analyses of F were performed using a second set of analytical conditions (60 nA), with counting times of 120 s on peak and 60 s for background⁵⁸. For glasses and minerals, we used the following standards for K α X-ray line calibration: albite for Na and Al, orthoclase for K, wollastonite for Si and Ca, TiO_2 for Ti, Fe_2O_3 for Fe, MgO for Mg, Mn_3O_4 for Mn, and CaSO_4 for SO_3 , CaF_2 for F. Raw data were corrected using the PAP routine. The precision for oxide concentrations was better than 1%. No significant alkali loss (within uncertainty) was detected during measurements.

Water determination. Raman spectra were recorded with a Jobin-Yvon LabRam HR800 spectrometer (grating: 2400 gr/mm), equipped with an Olympus optical microscope and a long-working-distance LMPanFI 100 \times /0.80 objective at GFZ Potsdam, Germany. We used a 488 nm excitation of a Coherent Ar + laser Model Innova 70C, a power of 180 mW (about 30 mW on sample), at a resolution <0.6 cm^{-1} . If necessary, the laser power was reduced by using density filters. Each unpolarized spectrum represents the accumulation of ten to twenty acquisitions of 10 seconds each. Spectra were collected at a constant laboratory temperature (20 °C) with a Peltier-cooled CCD detector, and the positions of the Raman bands were controlled and eventually corrected using the principal plasma lines in the Argon laser. The recommended and measured positions of the plasma lines in the fingerprint spectral region are not larger than 0.6 cm^{-1} . Water concentrations of the glasses were determined by confocal Raman spectroscopy following a standard method previously described in the literature^{59,60}. A fresh, polished synthetic glass with a total of 8.06 wt.% H_2O_T , determined by Karl Fischer titration, was used as a reference standard. The composition of this standard was cross-checked using about 30 different glasses of basaltic to granitic bulk composition. The standard glass has been polished before each series of measurements. At high water concentration the differences in the bulk composition disappear, and the H_2O -OH-Raman band is dominant. Because the integral intensity of the H_2O -OH stretching band between about 2800 and 4000 cm^{-1} increases directly, proportionally and linearly with the total water content it results a simple procedure for quantification, $I = 608 + 9219.15 \cdot \text{H}_2\text{O}_T$ ($r^2 = 0.9997$), in which I is measured integral intensity (a.u.). The uncertainty on the water concentration is given in Supplementary Data 1.

Data availability. The authors declare that all relevant data are available within the article and its supplementary information files.

Received: 30 October 2017 Accepted: 9 March 2018

Published online: 12 April 2018

References

- Frietsch, R. On the magmatic origin of iron ores of the Kiruna type. *Econ. Geol.* **73**, 478–485 (1978).
- Hildebrand, R. S. Kiruna-type deposits; their origin and relationship to intermediate subvolcanic plutons in the Great Bear magmatic zone, Northwest Canada. *Econ. Geol.* **81**, 640–659 (1986).
- Nyström, J. O. & Henriquez, F. Magmatic features of iron ores of the Kiruna type in Chile and Sweden; ore textures and magnetite geochemistry. *Econ. Geol.* **89**, 820–839 (1994).
- Gleason, J. D., Marikos, M. A., Barton, M. D. & Johnson, D. A. Neodymium isotopic study of rare earth element sources and mobility in hydrothermal Fe oxide (Fe-P-REE) systems. *Geochim. Cosmochim. Acta* **64**, 1059–1068 (2000).
- Naslund, H. R., Henriquez, F., Nyström, J. O., Vivallo, W. & Dobbs, F. M. in *Hydrothermal Iron Oxide Copper-gold and Related Deposits: A Global Perspective*, Vol. 2 (ed. Porter, T. M.) 207–226 (Porter Geoscience Consultancy Publishing, Adelaide, 2002).
- Sillitoe, R. H. & Burrows, D. R. New field evidence bearing on the origin of the El Laco magnetite deposit, northern Chile. *Econ. Geol.* **97**, 1101–1109 (2002).
- Chen, H., Clark, A. H. & Kyser, T. K. The Marcona magnetite deposit, Ica, South-Central Peru: a product of hydrous, iron oxide-rich liquids? *Econ. Geol.* **105**, 1441–1456 (2010).

8. Jonsson, E. et al. Magmatic origin of giant 'Kiruna-type' apatite-iron-oxide ores in Central Sweden. *Sci. Rep.* **3**, 1644 (2013).
9. Dare, S. A., Barnes, S. J. & Beaudoin, G. Did the massive magnetite "lava flows" of El Laco (Chile) form by magmatic or hydrothermal processes? New constraints from magnetite composition by LA-ICP-MS. *Miner. Depos.* **50**, 607–617 (2015).
10. Knipping, J. L. et al. Giant Kiruna-type deposits form by efficient flotation of magmatic magnetite suspensions. *Geology* **43**, 591–594 (2015).
11. Tornos, F., Velasco, F. & Hanchar, J. M. Iron-rich liquids, magmatic magnetite, and superheated hydrothermal systems: the El Laco deposit, Chile. *Geology* **44**, 427–430 (2016).
12. Nyström, J. O., Henriquez, F., Naranjo, J. A. & Nasuland, H. R. Magnetite spherules in pyroclastic iron ore at El Laco, Chile. *Am. Miner.* **101**, 587–595 (2016).
13. Mungall, J. E., Long, K., Brenan, J. M., Smythe, D. & Naslund, H. R. Immiscible shoshonitic and Fe-P-oxide melts preserved in unconsolidated tephra at El Laco volcano, Chile. *Geology* **46**, 255–258 (2018).
14. Velasco, F., Tornos, F. & Hanchar, J. M. Immiscible iron- and silica-rich melts and magnetite geochemistry at the El Laco volcano (northern Chile): evidence for a magmatic origin for the magnetite deposits. *Ore Geol. Rev.* **79**, 346–366 (2016).
15. Lindsley, D. & Epler, N. Do Fe-Ti-oxide magmas exist? Probably not! *Am. Miner.* **102**, 2157–2169 (2017).
16. Lester, G. W., Clark, A. H., Kyser, T. K. & Naslund, H. R. Experiments on liquid immiscibility in silicate liquids with H₂O, P, S, F and Cl: implications for natural magmas. *Contrib. Mineral. Petrol.* **166**, 329–349 (2013).
17. Philpotts, A. R. Compositions of immiscible liquids in volcanic rocks. *Contrib. Mineral. Petrol.* **80**, 201–218 (1982).
18. Charlier, B., Namur, O. & Grove, T. L. Compositional and kinetic controls on liquid immiscibility in ferrobasalt–rhyolite volcanic and plutonic series. *Geochim. Cosmochim. Acta* **113**, 79–93 (2013).
19. Charlier, B. & Grove, T. L. Experiments on liquid immiscibility along tholeiitic liquid lines of descent. *Contrib. Mineral. Petrol.* **164**, 27–44 (2012).
20. Bogaerts, M. & Schmidt, M. W. Experiments on silicate liquid immiscibility in the system Fe₂SiO₄-KAlSi₃O₈-SiO₂-CaO-MgO-TiO₂-P₂O₅ and implications for natural magmas. *Contrib. Mineral. Petrol.* **152**, 257–274 (2006).
21. Ryerson, F. J. & Hess, P. C. Implications of liquid-liquid distribution coefficients to mineral-liquid partitioning. *Geochim. Cosmochim. Acta* **42**, 921–932 (1978).
22. Longhi, J. Silicate liquid immiscibility in isothermal crystallisation experiments. *Proc. Lunar Planet. Sci. Conf.* **20**, 13–24 (1990).
23. Hess, P. C., Rutherford, M. J., Guillemette, R. N., Ryerson, F. J. & Tuschfeld, H. A. Residual products of fractional crystallisation of lunar magmas—an experimental study. *Proc. Lunar Planet. Sci. Conf.* **6**, 895–909 (1975).
24. Rutherford, M. J., Hess, P. C. & Daniel, G. H. Experimental liquid line of descent and liquid immiscibility for basalt 70017. *Proc. Lunar Planet. Sci. Conf.* **5**, 569–583 (1974).
25. Dixon, S. & Rutherford, M. J. Plagiogranites as late-stage immiscible liquids in ophiolite and mid-ocean ridge suites: an experimental study. *Earth. Planet. Sci. Lett.* **45**, 45–60 (1979).
26. Philpotts, A. R. & Doyle, C. D. Effect of magma oxidation state on the extent of silicate liquid immiscibility in a tholeiitic basalt. *Am. J. Sci.* **283**, 967–986 (1983).
27. Kamenetsky, V. S. et al. Magma chamber-scale liquid immiscibility in the Siberian Traps represented by liquid pools in native iron. *Geology* **41**, 1091–1094 (2013).
28. Hou, T. et al. Experimental study of liquid immiscibility in the Kiruna-type Vergenoeg iron–fluorine deposit, South Africa. *Geochim. Cosmochim. Acta* **203**, 303–322 (2017).
29. Namur, O., Charlier, B. & Holness, M. B. Dual origin of Fe-Ti-P gabbros by immiscibility and fractional crystallisation of evolved tholeiitic basalts in the Sept Iles layered intrusion. *Lithos* **154**, 100–114 (2012).
30. Fischer, L. A. et al. Immiscible iron- and silica-rich liquids in the upper zone of the Bushveld complex. *Earth. Planet. Sci. Lett.* **443**, 108–117 (2016).
31. Visser, W. & Koster van Groos, A. F. Effect of P₂O₅ and TiO₂ on liquid-liquid equilibria in the system K₂O-FeO-Al₂O₃-SiO₂. *Am. J. Sci.* **279**, 970–988 (1979).
32. Clark, A. H. & Kontak, D. J. Fe-Ti-P oxide melts generated through magma mixing in the Antauta subvolcanic center, Peru: implications for the origin of nelsonite and iron oxide-dominated hydrothermal deposits. *Econ. Geol.* **99**, 377–395 (2004).
33. Lyons, J. I. Volcanogenic iron oxide deposits, Cerro de Mercado and vicinity, Durango. *Econ. Geol.* **83**, 1886–1906 (1988).
34. Eslamizadeh, A. Petrology and geochemistry of early Cambrian volcanic rocks hosting the Kiruna-type iron ore in Anomaly 10 of Sechahun, Central Iran. *J. Sci. Islamic Repub. Iran.* **28**, 21–35 (2016).
35. Jiang, Z. et al. Geology, geochemistry, and geochronology of the zhibo iron deposit in the western Tianshan, NW China: constraints on metallogenesis and tectonic setting. *Ore Geol. Rev.* **57**, 406–424 (2014).
36. Jiang, Z. et al. Geochemistry and zircon U-Pb age of volcanic rocks from the chaganguoer and zhibo iron deposits, western Tianshan, and their geological significance. *Acta Petrol. Sin.* **28**, 2074–2088 (2012).
37. Mathez, E. A., VanTongeren, J. A. & Schweitzer, J. On the relationships between the Bushveld complex and its felsic roof rocks, part 1: petrogenesis of Rooiberg and related felsites. *Contrib. Mineral. Petrol.* **166**, 435–449 (2013).
38. Zajacz, Z. The effect of melt composition on the partitioning of oxidized sulfur between silicate melts and magmatic volatiles. *Geochim. Cosmochim. Acta* **158**, 223–244 (2015).
39. Wilke, M. Fe in magma—an overview. *Ann. Geophys.* **48**, 609–617 (2005).
40. Filiberto, J. et al. Effect of fluorine on near-liquidus phase equilibria of an Fe-Mg rich basalt. *Chem. Geol.* **312–313**, 118–126 (2012).
41. Lukkari, S. & Holtz, F. Phase relations of a F-enriched peraluminous granite: an experimental study of the Kymi topaz granite stock, southern Finland. *Contrib. Mineral. Petrol.* **153**, 273–288 (2007).
42. Kelley, K. A. & Cottrell, E. Water and the oxidation state of subduction zone magmas. *Science* **325**, 605–607 (2009).
43. Williams, P. et al. in *Economic Geology: One Hundredth Anniversary Volume* (eds Hedenquist, J. W., et al.) 371–406 (Society of Economic Geologists, Littleton, 2005).
44. Hitzman, M., Oreskes, N. & Einaudi, M. Geological characteristics and tectonic setting of proterozoic iron oxide (Cu-U-Au-REE) deposits. *Precam. Res.* **58**, 241–287 (1992).
45. Carmichael, I. S. E. The redox states of basic and silicic magmas: a reflection of their source regions? *Contrib. Mineral. Petrol.* **106**, 129–141 (1991).
46. Tornos, F., Velasco, F. & Hanchar, J. M. The magmatic to magmatic-hydrothermal evolution of the El Laco deposit (Chile) and its implications for the genesis of magnetite-apatite deposits. *Econ. Geol.* **112**, 1595–1628 (2017).
47. Burgisser, A. & Scaillet, B. Redox evolution of a degassing magma rising to the surface. *Nature* **445**, 194–205 (2007).
48. Bell, A. S. & Simon, A. Experimental evidence for the alteration of the Fe³⁺/ΣFe of silicate melt caused by the degassing of chlorine-bearing aqueous volatiles. *Geology* **39**, 499–502 (2011).
49. Moussallam, Y. et al. The impact of degassing on the oxidation state of basaltic magmas: a case study of Kilaua volcano. *Earth. Planet. Sci. Lett.* **450**, 317–325 (2016).
50. Berndt, J. et al. A combined rapid quench and H₂ membrane setup for internally heated pressure vessels: description and application for water solubility in basaltic liquids. *Am. Mineral.* **87**, 1717–1726 (2002).
51. Taylor, J. R., Wall, V. J. & Pownceby, M. I. The calibration and application of accurate redox sensors. *Am. Miner.* **77**, 284–295 (1992).
52. Huebner, J. S. & Sato, M. The oxygen fugacity-temperature relationships of manganese and nickel oxide buffers. *Am. Miner.* **55**, 934–952 (1970).
53. Botcharnikov, R. E., Koepke, J., Holtz, F., McCammon, C. & Wilke, M. The effect of water activity on the oxidation and structural state of Fe in a ferro-basaltic liquid. *Geochim. Cosmochim. Acta* **69**, 5071–5085 (2005).
54. Botcharnikov, R. E., Almeev, R. R., Koepke, J. & Holtz, F. Phase relations and liquid lines of descent in hydrous ferrobasalt—implications for the Skaergaard intrusion and Columbia river flood basalts. *J. Petrol.* **49**, 1687–1727 (2008).
55. Burnham, C. W. in *Volatiles in Magmas*. Reviews in Mineralogy Vol. 30 (eds Carroll, M. R. & Holloway, J. R.) 123–130 (Mineralogical Society of America, 1994).
56. Almeev, R. R. et al. High-temperature, low-H₂O silicic magmas of the yellowstone hotspot: an experimental study of rhyolite from the Bruneau-Jarbridge Eruptive Center, Central Snake River Plain, USA. *J. Petrol.* **53**, 1837–1866 (2012).
57. Schwab, R. G. & Küstner, D. Die gleichgewichtsfugazitäten technologisch und petrologisch wichtiger sauerstoffpuffer. *Neues Jahrb. für Mineral. Abh.* **140**, 111–142 (1981).
58. Zhang, C. et al. A practical method for accurate measurement of trace level fluorine in Mg- and Fe-bearing mineral and glass using electron probe microanalysis. *Geostand. Geoanal. Res.* **40**, 351–363 (2016).
59. Thomas, R. Determination of water contents of granite liquid inclusions by confocal laser Raman microprobe spectroscopy. *Am. Mineral.* **85**, 868–872 (2000).
60. Thomas, R., Kamenetsky, V. S. & Davidson, P. Laser Raman spectroscopy measurements of water in unexposed glass inclusions. *Am. Mineral.* **91**, 467–470 (2006).

Acknowledgements

Stefan Linsler, Julian Feige, and Chao Zhang are thanked for their help during experiments, sample preparation, and microprobe analyses. Don Lindsley is thanked for his kind help with the identification of oxide minerals. T.H. acknowledges support by the China Nature Foundation of Sciences (41502052 and 2016YFC0600502), a Marie Curie Individual Fellowship within the Horizon 2020—Research and Innovation Framework

Programme (656923), and the “Fundamental Research Funds for the Central Universities (2652015054)”. B.C. is a Research Associate of the Belgian Fund for Scientific Research-FNRS. O.N. was supported by an Emmy Noether grant (DFG NA1171/1-1). This work was partly supported by DFG grant KO1723/20-1 and Chinese 973 program (2012CB416806).

Author contributions

T.H., B.C., and O.N. designed the project, conducted the analyses, and led the writing of the manuscript. T.H. and O.N. conducted the experiments. R.T. analyzed the water concentrations in glasses. F.H., I.V., and Z.Z. contributed to the interpretation and did comprehensive editing.

Additional information

Supplementary Information accompanies this paper at <https://doi.org/10.1038/s41467-018-03761-4>.

Competing interests: The authors declare no competing interests.

Reprints and permission information is available online at <http://npg.nature.com/reprintsandpermissions/>

Publisher's note: Springer Nature remains neutral with regard to jurisdictional claims in published maps and institutional affiliations.



Open Access This article is licensed under a Creative Commons Attribution 4.0 International License, which permits use, sharing, adaptation, distribution and reproduction in any medium or format, as long as you give appropriate credit to the original author(s) and the source, provide a link to the Creative Commons license, and indicate if changes were made. The images or other third party material in this article are included in the article's Creative Commons license, unless indicated otherwise in a credit line to the material. If material is not included in the article's Creative Commons license and your intended use is not permitted by statutory regulation or exceeds the permitted use, you will need to obtain permission directly from the copyright holder. To view a copy of this license, visit <http://creativecommons.org/licenses/by/4.0/>.

© The Author(s) 2018